

www.acsami.org Research Article

Efficient and Stable Perovskite Solar Cells by B-Site Compositional **Engineered All-Inorganic Perovskites and Interface Passivation**

Lening Shen, Yongrui Yang, Tao Zhu, Lei Liu, Jie Zheng, and Xiong Gong*



Cite This: ACS Appl. Mater. Interfaces 2022, 14, 19469-19479



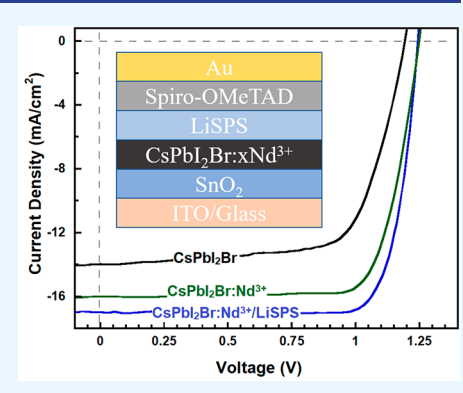
ACCESS I

Metrics & More

Article Recommendations

Supporting Information

ABSTRACT: Perovskite solar cells (PSCs) have emerged as a cost-effective solar technology in the past years. PSCs by three-dimensional hybrid inorganic-organic perovskites exhibited decent power conversion efficiencies (PCEs); however, their stabilities were poor. On the other hand, PSCs by all-inorganic perovskites indeed exhibited good stability, but their PCEs were low. Here, the development of novel allinorganic perovskites CsPbI₂Br:xNd³⁺, where Pb²⁺ at the B-site is partially heterovalently substituted by Nd3+, is reported. The CsPbI2Br:xNd3+ thin films possess enlarged crystal sizes, enhanced charge carrier mobilities, and superior crystallinity. Thus, the PSCs by the CsPbI₂Br:xNd³⁺ thin films exhibit more than 20% enhanced PCEs and dramatically boosted stability compared to those based on pristine CsPbI₂Br thin films. To further boost the device performance of PSCs, solution-processed 4-lithium styrenesulfonic acid/styrene copolymer (LiSPS) is utilized to passivate the surface defect and suppress surface charge carrier



recombination. The PSCs based on the CsPbI₂Br:xNd³⁺/LiSPS bilayer thin film possess reduced charge extraction lifetime and suppressed charge carrier recombination, resulting in 14% enhanced PCEs and significantly boosted stability compared to those without incorporation of the LiSPS interface passivation layer. All these results indicate that we developed a facile way to approach high-performance PSCs by all-inorganic perovskites.

KEYWORDS: perovskite solar cells, all-inorganic perovskites, compositional engineering, interface passivation, power conversion efficiency, stability

■ INTRODUCTION

Perovskite solar cells (PSCs) have drawn great attention in the past years due to the superior optoelectronic properties of perovskites and the feasibility of high-throughput manufacturing PSCs. 1-7 The PSCs based on the three-dimensional (3D) hybrid inorganic-organic perovskites with over 25% power conversion efficiencies (PCEs) have been reported.8 However, organic cations used to generate hybrid inorganic-organic perovskites are sensitive to moisture and oxygen. Thus, the PSCs based on 3D perovskites exhibited poor stability. 9,10 To boost the stability of PSCs, all-inorganic-based perovskites, where the organic cations were substituted by monovalent metal cations, such as Cs⁺ and K⁺, were developed. 11-17 Compared to those of hybrid inorganic-organic perovskites, all-inorganic-based perovskites possess relatively wide optical bandgaps, resulting in poor photovoltaic properties. 12,18-23 In addition, in all-inorganic-based perovskites, the cubic structure can be transferred to the orthorhombic structure quickly at a low temperature, resulting in even worse photovoltaic properties. 10,12,13 Great efforts have been paid to address these problems. 12,24-27 A PCE of 13.3% from the PSCs based on the phase-stabilized CsPbI₂Br has been reported by Mai et al.²⁵ Recently, the You group demonstrated PSCs with a PCE

of 18.22%, where the PSCs was fabricated by CsPbI_xBr_{3-x}/LiF bilayer thin film.²⁶

On the other hand, the studies demonstrated that partially substituted the B-site Pb2+ by other metal cations within perovskites could refine crystallization, stabilize crystal phases, tune dimensionality, and modify optoelectronic properties of perovskites. 5,6,28-32 We reported novel perovskites, $MAPb_{1-x}Co_xI_3$ (where $MA = CH_3NH_3^+$, and x = 0.1, 0.2, and 0.4 mol %), with tuned crystal structure (cubic rather than tetragonal) and boosted electrical conductivities.^{31,32} We further demonstrated that the PSCs based on the MAPb_{0.9}Co_{0.1}I₃ thin film exhibited a short-circuit current (J_{SC}) of 24.42 mA/cm², an open-circuit voltage (V_{OC}) of 1.07 V, and a fill factor (FF) of 82.0%, with a corresponding PCE of 21.43%, which is about 22% enhancement compared to those based on pristine MAPbI₃ thin film.³¹ Furthermore, studies illustrated that rare earth cations (RE³⁺) can reduce impurity

Received: February 2, 2022 Accepted: April 14, 2022 Published: April 23, 2022





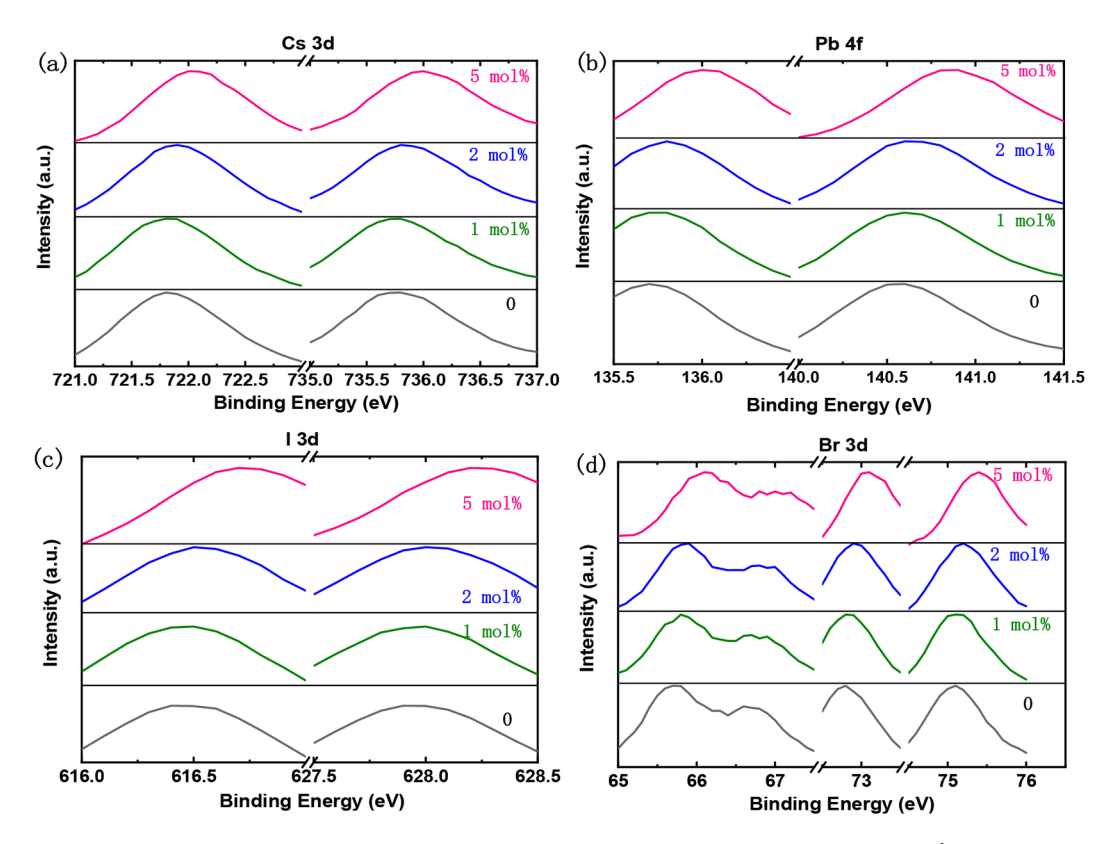


Figure 1. XPS spectra of (a) Cs 3d, (b) Pb 4f, (c) I 3d, and (d) Br 3d in pristine CsPbI₂Br and the CsPbI₂Br:xNd³⁺ (x = 1, 2, 5 mol %) thin films.

phases, eliminate deep defects, hamper chemical fluctuation, and improve film quality of the resultant RE3+-doped materials. 33-42 RE materials also possess great potential in optoelectronic applications owing to their unique physical properties. 40,41 For example, the Er- and Yb-doped NaYF₄ phosphors have been widely investigated in inorganic solar cells due to their unique up-conversion function to defeat the Shockley-Queisser limit for photovoltaic energy conversion efficiency. 42 Therefore, the heterovalent substitution of Pb2+ with $N\dot{d}^{3+}$ is anticipated to tune the vacancies at the B-site within perovskites by utilizing the low-lying 4f orbitals to boost the optoelectronic properties of the inorganic-based perovskites. 43,44 Toward this end, we have utilized Nd3+ to partially substitute Pb2+ for generating novel hybrid inorganic-organic perovskites, MAPbI₃:xNd³⁺ (where x = 0.1, 0.5, 1.0,and 5.0 mol %) and found the resultant perovskites possessed both enhanced and balanced charge transport. 6,32 Moreover, the PSCs based on the MAPbI₃:xNd³⁺ thin films exhibited a PCE of 21.15% and dramatically suppressed photocurrent hysteresis.^{6,32}

In this study, we report the development of novel allinorganic perovskites, CsPbI₂Br:xNd³⁺, where Pb²⁺ at the B-site is partially substituted by Nd³⁺. The CsPbI₂Br:xNd³⁺ thin films exhibit slightly enlarged optical gaps, significantly enlarged crystal sizes, enhanced charge carrier mobilities, and superior crystallinity compared to the pristine CsPbI₂Br thin film. Moreover, the PSCs based on the CsPbI₂Br:xNd³⁺ thin films exhibit more than 20% enhanced PCEs and boosted stability. To further boost device performance, 4-lithium styrenesulfonic acid/styrene copolymer (LiSPS) is utilized as the interface passivation layer. The PSCs based on the CsPbI₂Br:xNd³⁺/LiSPS bilayer thin film possess reduced charge extraction lifetime and suppressed charge carrier

recombination, resulting in 14% enhanced PCEs and dramatically boosted stability compared to those without incorporating with the LiSPS interface passivation layer.

MATERIALS AND METHODS

Materials. Lead iodide (99.9985%), lead bromide (99.999%), 2,2',7,7'-tetrakis(N,N-di-p-methoxyphenylamine)-9,9-spirobifluorene (Spiro-OMeTAD) (99%), 4-tert-butylpyridine (TBP) (96%), ethyl alcohol (≥99.5%), chlorobenzene (CB) (99.8%), dimethyl sulfoxide (DMSO) (≥99.9%), hydriodic acid (57 wt % in H₂O, 99.5%), molybdenum trioxide (MoO₃), and bis(trifluoromethane)sulfonimide lithium salt (Li-TFSI) (99.95%), and Au and Ag slugs were purchased from Sigma-Aldrich. Cesium iodide (99.9985%), tin(IV) oxide (15% in H₂O colloidal dispersion), and acetonitrile (ACN) (99.8%) were purchased from Alfa Aesar. C_{60} was purchased from Pure60OliveOil. Nd₂O₃ was purchased from Sinopharm Chemical Reagent Co., Ltd., China. All chemicals were used as received without further purification.

Preparation of Perovskite Thin Films. NdI3 was prepared by adding Nd2O3 into hydriodic acid with an accurate stoichiometric ratio in a 500 mL round-bottomed flask under vigorous stirring. The white powder was obtained by evaporating the solvent at 80 °C for 2 h in a vacuum. The powder was washed with ethanol and then dried under vacuum. For the CsPbI2Br precursor, 312 mg of CsI, 277 mg of PbI₂, and 220 mg of PbBr₂ were added to 1 mL of DMSO, and then the mixture was heated at 70 °C for ~1 h. For the CsPbI₂Br:xNd³⁺ precursor, different NdI3 was added into perovskite solution to tune the molar ratio of Pb²⁺ to Nd³⁺. Afterward, the precursor solution was filtered before further utilization. Both CsPbI₂Br and CsPbI₂Br:xNd³⁺ precursor solutions were preheated at 60 °C before making perovskite thin films. The final perovskite thin films were spin-casted from 50 μ L of corresponding precursor solutions at 3000 rpm for 30 s. Finally, perovskite thin films were first annealed at 45 °C for 2 min, at 100 °C for 2 min, and then at 200 °C for 5 min.

Characterization of Perovskite Thin Films. The characterization of the UV-vis absorption and photoluminescence (PL)

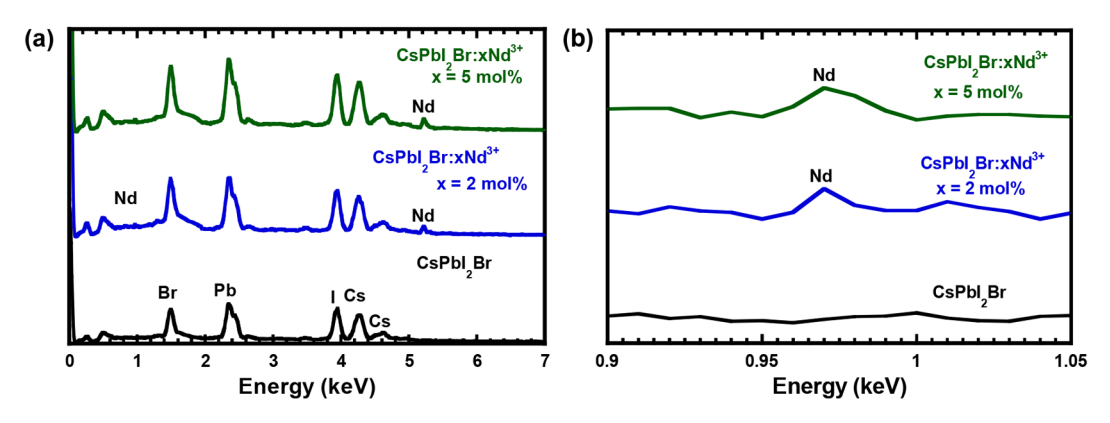
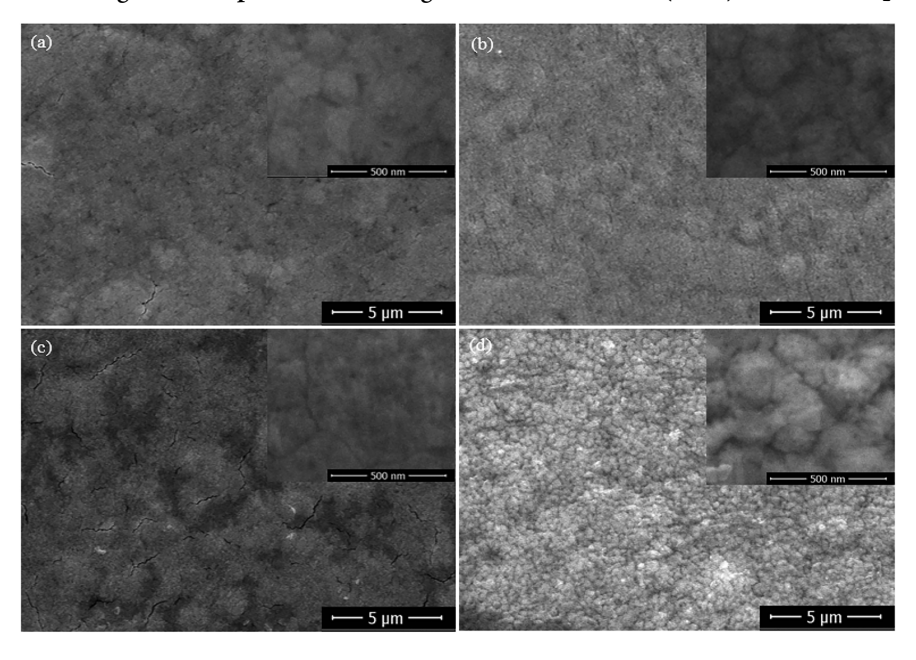


Figure 2. (a) EDS spectra of pristine $CsPbI_2Br$ thin film and the $CsPbI_2Br:xNd^{3+}$ (x = 2 or 5 mol %) thin films. (b) Details of the EDS spectra from 0.9 to 1.05 keV.

Scheme 1. Top-View SEM Images and Top-View SEM Images in a Smaller Scale (Inset) of the CsPbI₂Br:xNd³⁺ Thin Films^a



a(a) x = 0 mol %, (b) x = 1 mol %, (c) x = 2 mol %, and (d) x = 5 mol %, respectively.

spectra, X-ray photoelectron spectroscopy (XPS), scanning electron microscopy (SEM) images, energy-dispersive X-ray spectroscopy (EDS), and X-ray diffraction (XRD) of perovskite thin films followed the procedures described in our previous publications. 5-7,11,30,32,54,61,63 The grazing-incidence wide-angle X-ray scattering (GIWAXS) was performed on the high-resolution GIWAXS beamline (sector 8-ID-E) at Advanced Photon Source, Argonne National Laboratory. 46

Fabrication and Characterization of PSCs. The details of the procedures of fabrication and characterization of PSCs were described in our previous publications. 5-7,11,30,32,54,61,63

■ RESULTS AND DISCUSSION

In our previous studies, we found that MAPbI₃, where Pb²⁺ was partially substituted by Nd³⁺, possessed significantly enhanced and balanced charge carrier mobility, which resulted in boosted PCEs.⁶ However, the utilization of heterovalent substitution to tune charge transport of all-inorganic perovskites was rarely reported. In this study, Nd³⁺ is used to partially substitute Pb²⁺ within CsPbI₂Br to create novel CsPbI₂Br:xNd³⁺ perovskites. Nd³⁺ is selected for partial substitution of Pb²⁺ at the B-site within CsPbI₂Br since such

heterovalent substitution could generate the vacancy, resulting in tunable optoelectronic properties of the resultant perovskite. $^{45,47-49}$ Moreover, the RE $^{3+}$ cation is selected as the dopant since it can stabilize the phase and reduce crystal impurity. $^{23-42}$ Furthermore, Nd $^{3+}$ has been used to tune the optoelectronic properties of inorganic perovskite materials. 43 In addition, the ionic radii (112 pm) of Nd $^{3+}$ is similar to that (133 pm) of Pb $^{2+}$. Thus, the low-lying 4f orbital Nd $^{3+}$ is utilized to tune the vacancies at the B-site Pb $^{2+}$, and synergistically endowing the optoelectronic properties of perovskite materials is expected. $^{45,36,37,50-52}$

The whole XPS spectra of the CsPbI₂Br:xNd³⁺ (x = 0, 1, 2, and 5 mol %) thin films are shown in Figure S1. All components for the formation of the CsPbI₂Br:xNd³⁺ are found within perovskites. High resolution XPS spectra of the CsPbI₂Br:xNd³⁺ (x = 0, 1, 2, and 5 mol %) thin films are displayed in Figure 1. The typical features of Cs, Pb, I, and Br are observed from all thin films, which further confirm the formation of the CsPbI₂Br:xNd³⁺ thin films. However, compared to pristine CsPbI₂Br thin film, the binding energies (BE) of the Cs 3d of the CsPbI₂Br:xNd³⁺ thin films are

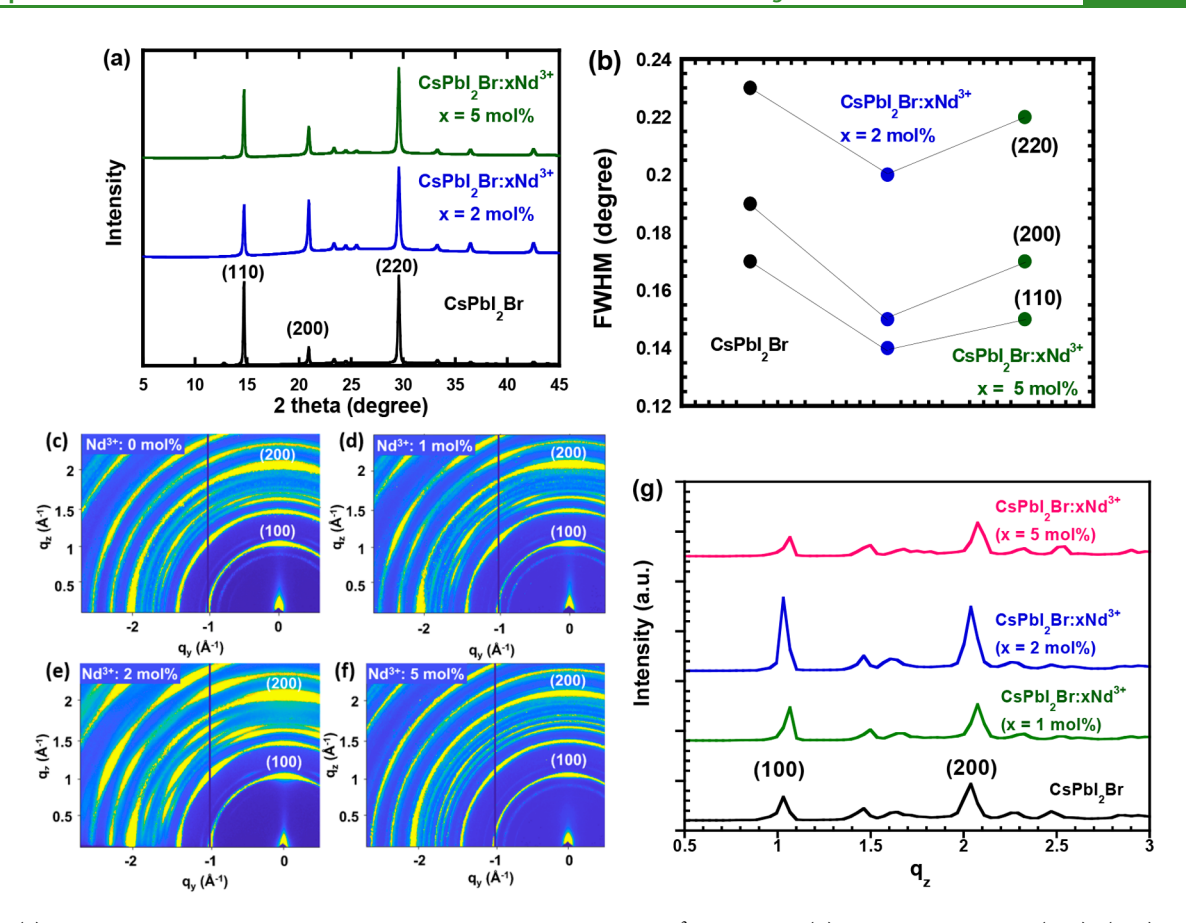


Figure 3. (a) XRD patterns of pristine $CsPbI_2Br$ thin film and the $CsPbI_2Br:xNd^{3+}$ thin films. (b) The fwhm values of (110), (200), and (220) plans of pristine $CsPbI_2Br$ thin film and the $CsPbI_2Br:xNd^{3+}$ thin films. GIWAXS profiles of (c) pristine $CsPbI_2Br$ thin film and (d-f) $CsPbI_2Br:xNd^{3+}$ (x = 1%, 2%, and 5%) thin films. (g) Intensity of GIWAXS profiles of (c)–(f) in the direction out of the plane of the $CsPbI_2Br:xNd^{3+}$ (x = 0%, 2%, and 5%) thin films.

increased along with increased doping concentrations of Nd³⁺. For example, the BE is increased from 0.10 eV for the $CsPbI_2Br:xNd^{3+}$ (x = 2 mol %) thin film to 0.20 eV for the $CsPbI_2Br:xNd^{3+}$ (x = 5 mol %) thin film. These results demonstrate that the Cs+ chemical environment is tuned by different concentrations of Nd3+, indicating that there is a chemical interaction between Cs⁺ and Nd³⁺ and such interaction is more intense along with increased doping concentrations of Nd³⁺. Moreover, similar phenomena are observed for Pb 4f, I 3d, and Br 3d. For example, the BEs for Pb 4f are slightly increased from 0.10 eV for the CsPbI₂Br:xNd³⁺ (x = 2 mol %) thin film to 0.30 eV for the CsPbI₂Br:xNd³⁺ (x = 5 mol %) thin film. The BEs of I 3d and Br 3d are increased from 0.20 eV for the CsPbI₂Br:xNd³⁺ (x =2 mol %) thin film to 0.40 eV for the CsPbI₂Br:xNd³⁺ (x = 5mol %) thin film. These results demonstrate that the Pb²⁺, I⁻, and Br chemical environments are also tuned by different concentrations of Nd3+, further indicating that there are chemical interactions between Pb2+, I-, and Br and Nd3+, respectively, and such chemical interactions are more intense along with increased doping concentrations of Nd³⁺. The above results demonstrate that Pb2+ at the B-site is indeed heterovalently substituted by Nd³⁺.

To further verify the interaction between Nd^{3+} and Cs^+ , Pb^{2+} , I^- , and Br^- , the EDS measurements of both pristine $CsPbI_2Br$ and the $CsPbI_2Br:xNd^{3+}$ (where x=2 or 5 mol %) thin films are performed, and the results are shown in Figure 2. The peaks of Cs^+ (4.28 and 4.61 keV), Pb^{2+} (2.34 keV), I^-

(3.94 keV), and Br⁻ (1.48 keV) presented in all these three samples confirm that Nd³⁺ is indeed within perovskites. Moreover, a peak of the Nd³⁺ (5.23 keV) is observed from the CsPbI₂Br:xNd³⁺ (x = 2 or 5 mol %) thin films, whereas no peak, corresponding to the Nd³⁺ (5.23 keV), is observed from the pristine CsPbI₂Br thin film. In addition, as indicated in Figure 2b, a peak located at 0.97 keV, which is also corresponding to Nd³⁺, is observed from the CsPbI₂Br:xNd³⁺ (x = 2 or 5 mol %) thin films, but no peak located at 0.97 keV is found in the pristine CsPbI₂Br thin film. However, the concentration of Nd³⁺ is very low, which brings a difficult to map Nd³⁺ in the CsPbI₂Br:xNd³⁺ (x = 2 or 5 mol %) thin films

Scheme 1 shows the top-view SEM images of the $CsPbI_2Br:xNd^{3+}$ (x=0, 1, 2, and 5 mol %) thin films. The $CsPbI_2Br:xNd^{3+}$ thin films exhibit significantly different film morphology compared to pristine $CsPbI_2Br$ thin film. The perovskite crystal size distributions within thin films are different (Figure S2). The average crystal size of pristine $CsPbI_2Br$ thin films ~ 150 nm. The average crystal sizes of the $CsPbI_2Br:xNd^{3+}$ thin films are enlarged to ~ 250 nm for the $CsPbI_2Br:xNd^{3+}$ (x=1 mol %) thin film and ~ 300 nm for the $CsPbI_2Br:xNd^{3+}$ (x=2 mol %) thin film and then reduced to ~ 200 nm for the $CsPbI_2Br:xNd^{3+}$ (x=5% mole) thin film. The largest size of ~ 300 nm is observed from the $CsPbI_2Br:xNd^{3+}$ (x=2 mol %) thin film. In addition, compared to other perovskite thin films, a rough surface is also observed from the $CsPbI_2Br:xNd^{3+}$ (x=5 mol %) thin film.

These results imply that the crystal nucleation in these perovskites is different.

The XRD patterns of pristine CsPbI₂Br and the CsPbI₂Br:xNd³⁺ thin films are shown in Figure 3a. The peaks are located at 2θ of 14.71°, 20.90°, and 29.58°, which corresponds to the (110), (200), and (220) planes, indicating that both pristine CsPbI₂Br and the CsPbI₂Br:xNd³⁺ thin films possess the tetragonal crystal structure and the Nd³⁺ substitution of Pb²⁺ did not tune the crystal structure of the CsPbI₂Br thin film. Moreover, it is found that the peak intensities of these plans are increased along with Nd³⁺ doping concentrations, which indicates that these samples have different crystallinities. To quantify the difference in crystallinity, the full width at half-maximum (fwhm) values of the (110), (200), and (220) planes are calculated, and the results are shown in Figure 3b and summarized in Table 1. The

Table 1. Full Width at Half-Maximum Values of Perovskite Thin Films

	plane		
perovskite	(110)	(200)	(220)
CsPbI ₂ Br	0.17°	0.19°	0.23°
CsPbI ₂ Br:Nd ³⁺ (2 mol %)	0.14°	0.15°	0.20°
CsPbI ₂ Br:Nd ³⁺ (5 mol %)	0.15°	0.17°	0.22°

smallest fwhm values of the (110), (200), and (220) planes observed from the $CsPbI_2Br:xNd^{3+}$ (x=2 mol %) demonstrate that such perovskite possesses the highest crystallinity among the $CsPbI_2Br:xNd^{3+}$ (x=0,1,2, and 5 mol %) thin films.

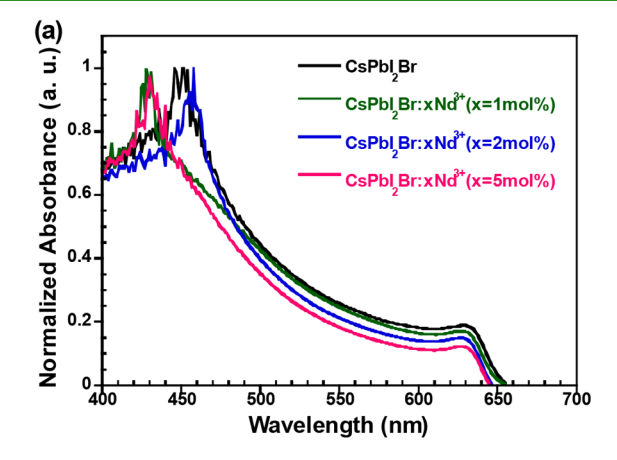
Figure 3c-f presents the GIWAXS profiles of the $CsPbI_2Br:xNd^{3+}$ (x=0,1,2, and 5 mol %) thin films. Pristine $CsPbI_2Br$ thin film shows a relatively random orientation with strongly scattered rings in all reflections along with the scattering vector, whereas the mixture of secondary spots and rings is observed from the $CsPbI_2Br:xNd^{3+}$ (x=1,2, and 5 mol %) thin films. These results indicate that the dominant crystallites within the $CsPbI_2Br:xNd^{3+}$ thin films are those oriented (100) and (200) planes and the $CsPbI_2Br:xNd^{3+}$ thin films possess a better crystallinity compared to pristine $CsPbI_2Br$ thin film.

Figure 3g displays the GIWAXS profiles, which are the intensities of the peak in the direction out of the plane. Compared to pristine CsPbI₂Br thin film, increased intensities

of the (100) and (200) planes are observed from the $CsPbI_2Br:xNd^{3+}$ thin films. Such increased intensity is more pronounced in the $CsPbI_2Br:xNd^{3+}$ thin film as the doping concentration of Nd^{3+} is at 2 mol %. These results further confirm that Pb^{2+} is indeed partially substituted by Nd^{3+} at the B-site and the resultant perovskite thin films possess a superior crystallinity. The boosted crystallinity observed from the $CsPbI_2Br:xNd^{3+}$ (x=2 mol %) thin film is probably attributed to the vacancies at the B-site Pb^{2+} created by the low-lying 4f orbitals of Nd^{3+} , $^{41-45}$ resulting in a distortion of the $[Pb(I_2Br)_6]^{4-}$ octahedra. Thus, tunable electronic properties are anticipated to be observed from the $CsPbI_2Br:xNd^{3+}$ thin films.

Figure 4a,b presents the absorption and photoluminescence (PL) spectra of pristine CsPbI₂Br and the CsPbI₂Br:xNd³⁺ thin films. It is found that the absorption spectra of the CsPbI₂Br:xNd³⁺ thin films are slightly blue-shifted along with increased Nd3+ doping concentrations. The optical gaps, calculated based on the cutoff of absorption spectra, are 1.899 eV, 1.908 eV, 1.922 eV, and 1.931 eV for pristine CsPbI₂Br, the CsPbI₂Br:xNd³⁺ (x = 1 mol %), the $CsPbI_2Br:xNd^{3+}$ (x = 2 mol %), and the $CsPbI_2Br:xNd^{3+}$ (x= 5 mol %) thin films, respectively. The optical gaps are slightly enlarged along with increased doping concentrations of Nd³⁺. Similar to the absorption spectra, the PL spectra of the CsPbI₂Br:xNd³⁺ thin films are blue-shifted along with increased doping concentrations of Nd3+. Such blue-shifted absorption and PL spectra are attributed to Pb2+ partially replaced by Nd3+, which results in different electronic band structures and enlarged bandgaps.⁶ Moreover, Nd³⁺ in the CsPbI₂Br lattice probably enhances the lattice volume and tunes the total superposition of electron wave functions in the CsPbI₂Br:xNd³⁺ lattice.⁶ In addition, the low-lying 4f orbitals of Nd³⁺ probably could induce a distortion of the [Pb- $(I_xBr_{1-x})_6$ ⁴⁻ octahedra and boosted the density of state, resulting in enlarged bandgaps of the CsPbI₂Br:xNd³⁺ thin films. 5,6,41-45,50-52

Figure 5a,b presents the current versus voltage (I-V) characteristics of the electron-only diodes with a device structure of ITO/SnO₂/perovskite/C₆₀/Ag and the holey only diodes with a device structure of ITO/MoO₃/perovskite/Spiro-OMeTAD/Ag, where ITO and Ag act as the electrodes, SnO₂ and C₆₀ are used as the electron transport layer, MoO₃ and Spiro-OMeTAD are used as the hole



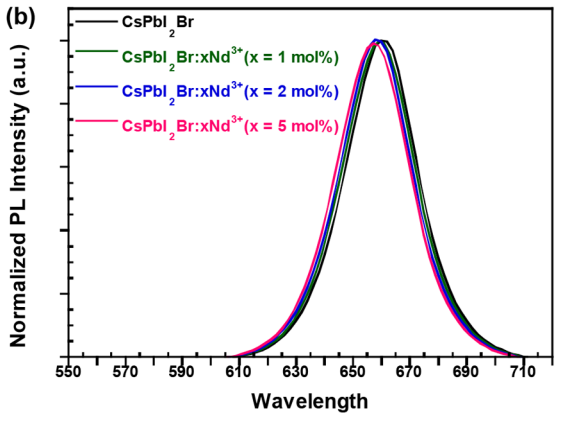


Figure 4. (a) Steady-state absorption and (b) photoluminescence (PL) spectra of pristine $CsPbI_2Br$: xNd^{3+} (x = 1, 2, and 5 mol%) thin films.

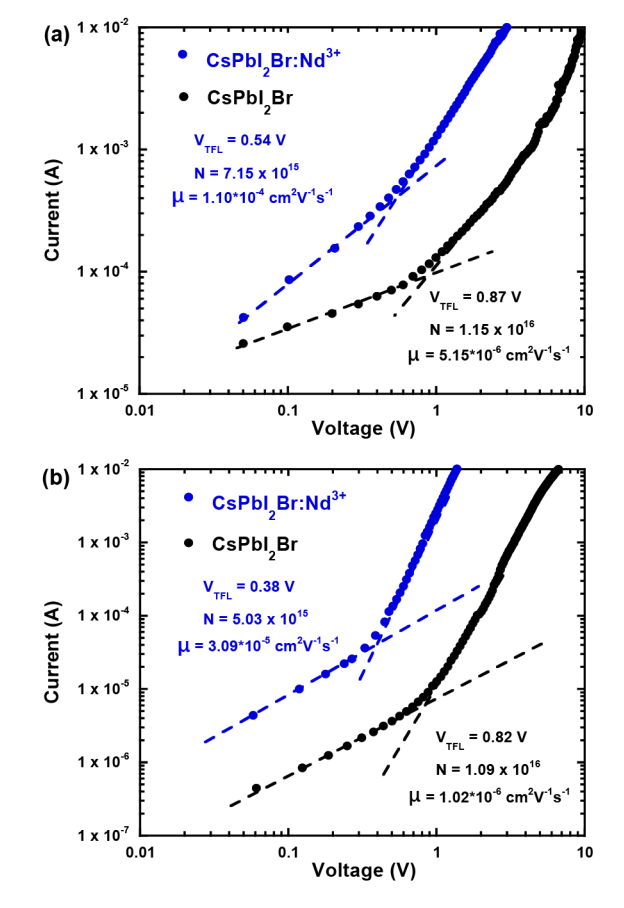


Figure 5. I-V characteristics of (a) the electron-only device and (b) the hole-only device fabricated by either pristine CsPbI₂Br thin film or the CsPbI₂Br:Nd³⁺ thin film, respectively.

transport layer, and the perovskite layer is either pristine $CsPbI_2Br$ or the $CsPbI_2Br:xNd^{3+}$ thin film (x = 2 mol %), respectively. It is found that the CsPbI2Br:xNd3+ thin film possesses different trap-filled limit voltages (V_{TFL}) compared to pristine CsPbI2Br thin film. For the electron transport, the V_{TFL} values are reduced to 0.54 V for the CsPbI₂Br:xNd³⁺ thin film from 0.87 V for pristine CsPbI₂Br thin film, and for the hole transport, the V_{TFL} values are dropped to 0.38 V for the CsPbI₂Br:xNd³⁺ thin film from 0.82 V for pristine CsPbI₂Br thin film. The trap density (N_t) is described as N_t = $(2\varepsilon_0 \varepsilon V_{TFL})/(eL^2)$ (where L is the thickness of the active layer, ε_0 is the vacuum permittivity (8.85 × 10⁻¹² C·V⁻¹·m⁻¹), ε is the relative dielectric constant of the active layer, and e is the elementary electric charge). The ε values are calculated to be 40.70 and 43.51 for pristine CsPbI2Br thin film and the CsPbI₂Br:xNd³⁺ thin film, respectively, which are based on the capacitance versus frequency (C-F) characteristics (Figure S3). The film thickness of both pristine CsPbI₂Br and the CsPbI₂Br:xNd³⁺ thin films is measured to be ~500 nm. Thus, hole-trap and electron-trap densities for pristine CsPbI2Br thin film are estimated to be 1.09×10^{16} cm⁻³ and 1.15×10^{16} cm⁻³, respectively, whereas for the CsPbI₂Br:xNd³⁺ thin film, the hole-trap and electron-trap densities are estimated to be 5.03×10^{15} cm⁻³ and 7.15×10^{15} cm⁻³, respectively. Both the hole-trap and electron-trap densities of the CsPbI₂Br:xNd³⁺ thin film are 10 times smaller than those for pristine CsPbI₂Br thin film. Such reduced trap densities are ascribed to the reduced point-defect at the atomic scale and the larger crystal

grain size with fewer grain boundaries induced by Nd³⁺ substitutions (Scheme 1).⁶

On the basis of the Mott-Gurney law,⁵³ the charge carrier mobility is described as $\mu=\frac{8JL^3}{9\varepsilon\varepsilon_0V^2}$ (where μ is charge carrier mobility, L is the thickness of the active layer, ε_0 is the vacuum permittivity, ε is the relative dielectric constant for the active layer, *J* is the current density, and *V* is the external bias). Thus, the electron and hole mobilities are calculated to be 5.15 \times $10^{-6}~\text{cm}^2~\text{V}^{-1}~\text{s}^{-1}$ and $1.02~\text{X}~10^{-6}~\text{cm}^2~\text{V}^{-1}~\text{s}^{-1}$ for pristine CsPbI₂Br thin film, respectively, whereas the electron and hole mobilities are calculated to be $1.10 \times 10^{-4} \text{ cm}^2 \text{ V}^{-1} \text{ s}^{-1}$ and $3.09 \times 10^{-5} \text{ cm}^2 \text{ V}^{-1} \text{ s}^{-1}$ for the CsPbI₂Br:xNd³⁺ thin film, respectively. The CsPbI₂Br:xNd³⁺ thin film possesses both significantly enhanced electron and hole mobilities compared to pristine CsPbI₂Br thin film. Such boosted charge carrier mobilities are attributed to the significantly reduced electron and hole trap densities and enlarged crystal sizes induced by Nd³⁺ substitutions.

The photovoltaic properties of the CsPbI₂Br:xNd³⁺ (x = 0, 1, 2, and 5 mol %) thin films are investigated through the characterization of the PSCs with a device structure of ITO/SnO₂/perovskites/Spiro-OMeTAD/Au (where the perovskite layer is either pristine CsPbI₂Br or the CsPbI₂Br:xNd³⁺ thin films and Au is used as the anode), under white light illumination with the light intensity of 100 mW/cm². The device performance parameters of PSCs are summarized in Table 2. The J-V characteristics of PSCs are shown in Figure

Table 2. Device Performance Parameters of PSCs

photoactive layer	$V_{ m OC} \ m (V)$	J_{SC} (mA/cm ²)	FF (%)	PCE (%)
CsPbI ₂ Br	1.20	13.97	69	11.60
CsPbI2Br:xNd3+ (x = 1 mol %)	1.20	14.48	73	12.59
CsPbI2Br:xNd3+ (x = 2 mol %)	1.25	16.01	75	15.01
CsPbI2Br:xNd3+ (x = 5 mol %)	1.16	11.94	69	9.51

S4. It is found that PCEs values of PSCs are increased and then decreased along with the increased doping concentrations of Nd³⁺. The best device performance is observed from the PSCs based on the CsPbI₂Br:xNd³⁺ thin film, where the Nd³⁺ doping concentration is at 2 mol %. The decreased PCEs originate from the rough surface and surface defects of the resultant perovskite thin film (Scheme 1).

To further optimize the device performance, LiSPS is used as the interface passivation layer on the top of the perovskite layer since LiSPS can passivate the interface defects of solution-processed perovskite thin film.⁵⁴ LiSPS is an ultrathin ionomer layer, which was applied to re-engineer the interface between the perovskite layer and spiro-OMeTAD layer in the PSCs devices. The optimized contact between the two layers by the modification with a LiSPS layer results in a reduced charge-carrier recombination. Moreover, LiSPS can also fill the traps at the surface of the perovskite layer to decrease the current leakage and improve the stability of the PSCs devices. The device performance of PSCs incorporated with different thicknesses of the LiSPS interface passivation layer is summarized in Table S1. Figure 6a presents the J-V characteristics of the PSCs based on either pristine CsPbI2Br thin film or the CsPbI₂Br:xNd³⁺ thin film or the

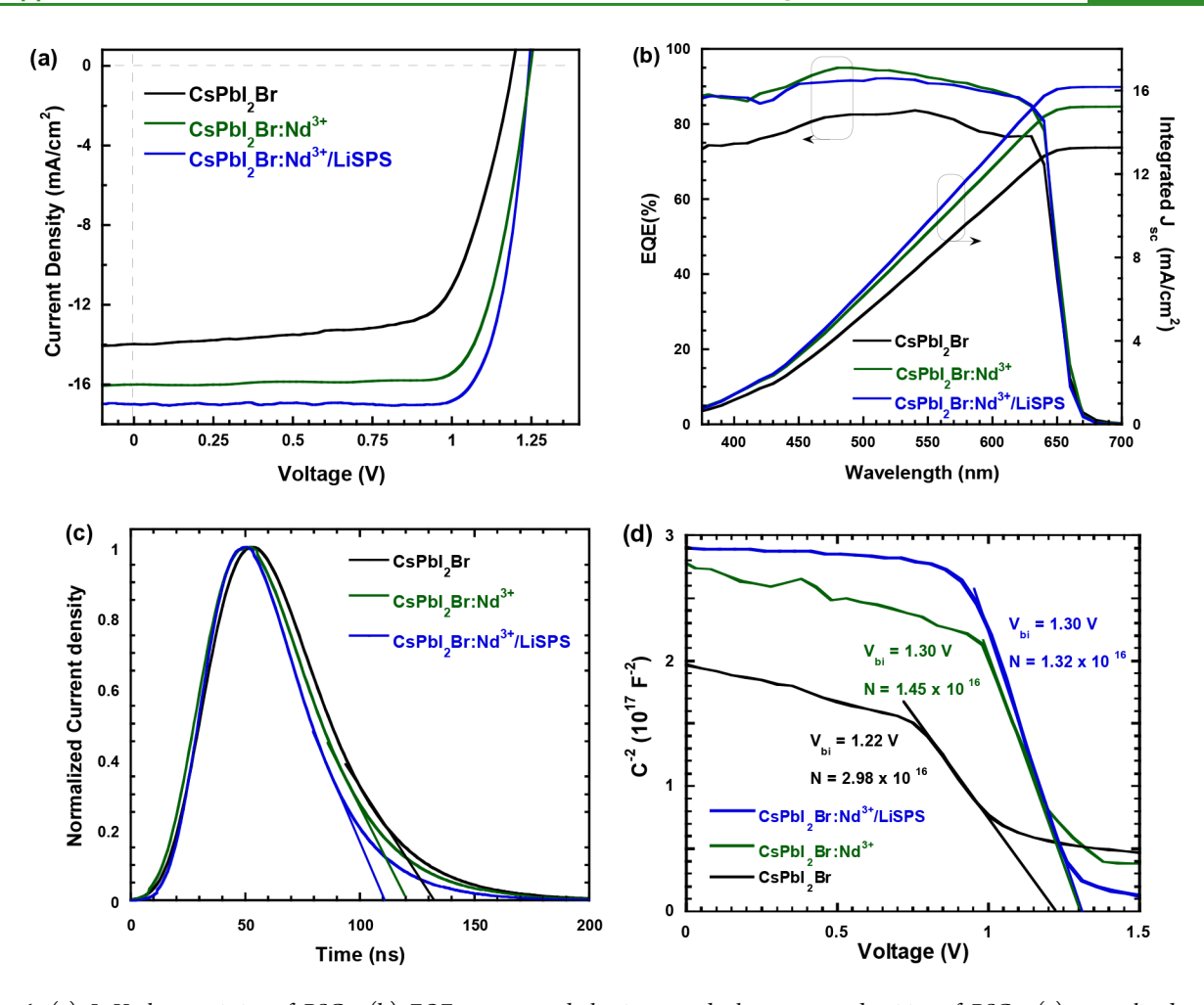


Figure 6. (a) J-V characteristics of PSCs, (b) EQE spectra and the integrated photocurrent densities of PSCs, (c) normalized transient photocurrent curves of PSCs, and (d) C-V characteristics of PSCs, where PSCs are with the same device structure but with different photoactive layers: pristine CsPbI₂Br thin film, the CsPbI₂Br:Nd³⁺ thin film, and the CsPbI₂Br:Nd³⁺/LiSPS bilayer thin film.

CsPbI₂Br:xNd³⁺/LiSPS bilayer thin film. The PSCs based on pristine CsPbI₂Br thin film exhibit a $V_{\rm OC}$ of 1.20 V, a $J_{\rm SC}$ of 13.97 mA/cm², and a FF of 69% and with a corresponding PCE of 11.60%. The PSCs based on the CsPbI₂Br:xNd³⁺ (x =2 mol %) thin film exhibit a $V_{\rm OC}$ of 1.25 V, a $J_{\rm SC}$ of 16.01 mA/ cm², and a FF of 75% and with a corresponding PCE of 15.01%, which is more than 20% enhancement compared to that based on pristine CsPbI2Br thin film. Such enhanced PCEs are ascribed to the boosted charge carrier mobility and enlarged crystal size of the CsPbI₂Br:xNd³⁺ thin film. Furthermore, the PSCs based on the CsPbI₂Br:xNd³⁺/LiSPS bilayer thin film exhibit a $V_{\rm OC}$ of 1.25 V, a $J_{\rm SC}$ of 16.98 mA/ cm², and a FF of 81%, with a corresponding PCE of 17.05%, which is approximately 14% enhancement compared to that without incorporating the LiSPS interface passivation layer. These results illustrate that the surface defects of the CsPbI₂Br:xNd³⁺ thin film are passivated by the LiSPS interface passivation layer, resulting in suppressed charge recombination and thus boosted PCEs.

Figure 6b displays the EQE of PSCs and the integrated J_{SC} , which are based on the EQE spectra of PSCs. Boosted EQE values are observed from the PSCs based on either the CsPbI₂Br:xNd³⁺ thin film or the CsPbI₂Br:xNd³⁺/LiSPS bilayer thin film. The highest EQE values (90%) ranging from 450 to 600 nm are observed from the PSCs based on the

CsPbI₂Br:xNd³⁺/LiSPS bilayer thin film. The integrated J_{SC} values are 13.28 mA/cm², 15.23 mA/cm², and 16.18 mA/cm² for the PSCs based on either pristine CsPbI₂Br or the CsPbI₂Br:xNd³⁺ or the CsPbI₂Br:xNd³⁺/LiSPS bilayer thin films, respectively. These integrated J_{SC} values are in good agreement with those extracted from the J-V characteristics (Figure 6a). All these results further prove the contribution of enhanced charge mobility and enlarged crystal size of the CsPbI₂Br:xNd³⁺ thin film and the functionality of the LiSPS interface passivation layer.

The TPC measurement is conducted to investigate the charge generation and transport kinetics in PSCs. S5,56 Figure 6c presents the normalized TPC curves of PSCs. Under the short-circuit condition, all PSCs possess a similar transient photocurrent curve. In the beginning, the TPC curves tended to be linear because most of the charge carriers are extracted during a significantly short time. However, a significant difference has happened after ~50 ns. Such differences originated from the trap and detrap processes of charge carriers. Through extrapolation of the linear region to zero, the lifetime of charge extraction is estimated. The charge extraction lifetime of 100 ns is observed from the PSCs based on the CsPbI₂Br:xNd³⁺/LiSPS bilayer thin film, whereas the charge extraction lifetimes of 122 and 132 ns are observed from the PSCs based on the CsPbI₃Br:xNd³⁺ thin film and the

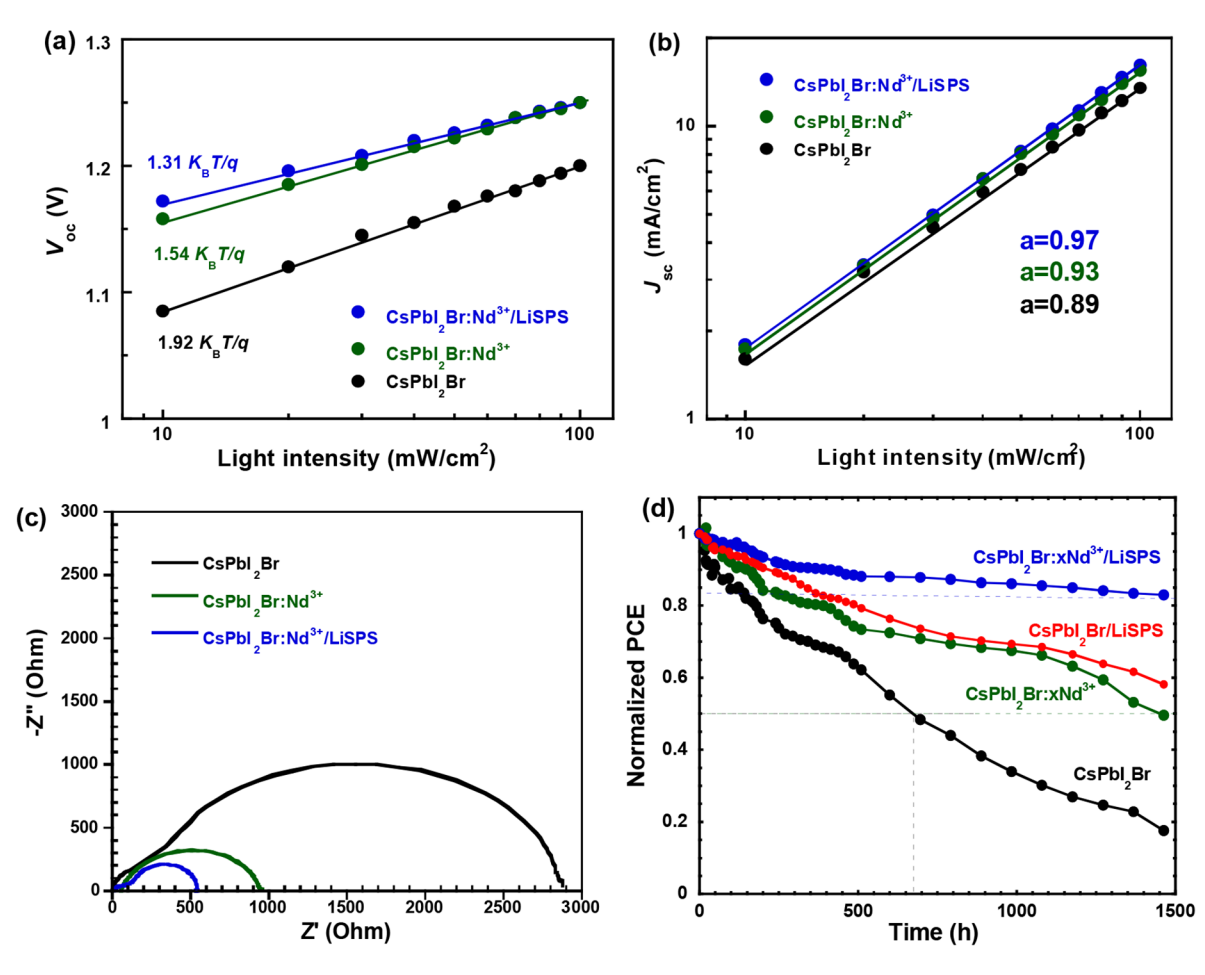


Figure 7. Light intensity dependent on (a) $V_{\rm OC}$ and (b) $J_{\rm SC}$ of PSCs, (c) Nyquist plot of (in dark) PSCs, and (d) the shelf-stability of unencapsulated PSCs, where the PSCs are with the same device structure, but with different photoactive layers: pristine CsPbI₂Br thin film, the CsPbI₂Br:Nd³⁺ thin film, and the CsPbI₂Br:Nd³⁺/LiSPS bilayer thin film.

PSCs based on pristine $CsPbI_2Br$ thin film. A short charge extraction lifetime indicates a fast sweep-out process of the charge carrier. Thus, the PSCs based on the $CsPbI_2Br:xNd^{3+}$ thin film exhibit enlarged J_{SC} . Compared to the PSCs based on pristine $CsPbI_2Br$ thin film, increased photocurrent densities observed from the PSCs based on the $CsPbI_2Br:xNd^{3+}$ thin film and from the PSCs based on the $CsPbI_2Br:xNd^{3+}/LiSPS$ bilayer thin film (Figure SS) further indicate suppressed charge carrier recombination and enhanced charge carrier mobility of the $CsPbI_2Br:xNd^{3+}$ thin film and suppressed surface defects by the LiSPS interface passivation layer.

The Mott–Schottky analysis ^{53,57} is further used to investigate the charge carrier behavior of PSCs. Figure 6d shows the C-V characteristics of PSCs. On the basis of the slope of the linear fitting of the C^{-2} versus V curves, the trap density (N) is estimated. ^{53,58} N values of 1.32×10^{16} cm⁻³, 1.45×10^{16} cm⁻³, and 2.98×10^{16} cm⁻³ are estimated for the PSCs based on the $CsPbI_2Br:xNd^{3+}/LiSPS$ bilayer, the $CsPbI_2Br:xNd^{3+}$ and pristine $CsPbI_2Br:xNd^{3+}$ thin films, respectively. Suppressed trap density indicates that PSCs exhibit large J_{SC} , thus high PCE. On the other hand, the built-in potential (V_{bi}) is estimated by extrapolating the linear fitting line to the intercept on the bias axis. A V_{bi} of 1.30 V is observed from the PSCs based on the $CsPbI_2Br:xNd^{3+}/LiSPS$ bilayer thin film, and a similar value to the above V_{bi} is observed from the PSCs based on the $CsPbI_2Br:xNd^{3+}$ thin

film. A $V_{\rm bi}$ of 1.22 V is observed from the PSCs based on pristine CsPbI₂Br thin film. Therefore, the PSCs based on either the CsPbI₂Br:xNd³⁺/LiSPS bilayer thin film or the CsPbI₂Br:xNd³⁺ thin film exhibit a larger $V_{\rm OC}$ compared to that based on pristine CsPbI₂Br thin film.

The light intensity-dependent J_{SC} and V_{OC} are further investigated to understand the underlying of enhanced $J_{\rm SC}$. Significant Figure 7a shows the light intensity versus $V_{\rm OC}$ of PSCs. Under the open-circuit condition, $V_{\rm OC}$ has been described as $V_{\rm OC} = n(K_{\rm b}T/q)\ln(I)^{62,63}$ (where $K_{\rm b}$ is the Boltzmann constant, T is the temperature in kelvin, q is the elementary charge, and n is a constant). As n equals 1, the bimolecular recombination is dominant in solar cells, whereas as n equals 2, the monomolecular recombination is dominant in solar cells. The slopes of $1.92K_bT/q$, $1.54K_bT/q$, and $1.31K_bT/q$ are observed from the PSCs based on either pristine CsPbI₂Br thin film or the CsPbI₂Br:xNd³⁺ thin film or the CsPbI₂Br:xNd³⁺/LiSPS bilayer thin film, respectively. Thus, compared to the PSCs based on pristine CsPbI₂Br thin film, a weaker monomolecular charge recombination process takes place within the PSCs based on the CsPbI₂Br:xNd³⁺ thin film, and an even more suppressed monomolecular charge recombination process takes place within the PSCs based on the CsPbI₂Br:xNd³⁺/LiSPS bilayer thin film. Therefore, these two PSCs exhibit larger J_{SC} and PCEs.

Figure 7b shows the light intensity versus J_{SC} of PSCs. J_{SC} related to the light intensity is described as $J_{SC} \in I^{a 64}$ (where Iis the light intensity and a is the coefficient). A large a indicates that a weaker charge carrier recombination happens in solar cells. All PSCs possess a power-law dependence of J_{SC} on the light intensity. The PSCs based on the CsPbI₂Br:xNd³⁺/LiSPS bilayer thin film exhibit an a of 0.97, which is larger than that (0.93) observed from the PSCs based on the CsPbI₂Br:xNd³⁺ thin film. The latter one is larger than that (0.89) from the PSCs based on pristine CsPbI2Br thin film. Thus, the PSCs based on the CsPbI₂Br:xNd³⁺/LiSPS bilayer thin film exhibit the best device performance among these three PSCs.

To understand the overall enhancement in FF, the IS spectra measured in the dark have been carried out to monitor the detailed electric properties of PSCs, which cannot be directly observed from the J-V characteristics. Figure 7c presents the Nyquist plot of PSCs. The charge-transfer resistance (R_{CT}) values for the PSCs based on either pristine CsPbI₂Br thin film or the CsPbI₂Br:xNd³⁺ thin film or the CsPbI₂Br:xNd³⁺/LiSPS bilayer thin film are estimated to be ${\sim}3000~\Omega$, ${\sim}950~\Omega$, and ~550 Ω , respectively. The smaller $R_{\rm CT}$ originates from highquality film and suppressed charge carrier recombination. Thus, the PSCs based on the CsPbI₂Br:xNd³⁺/LiSPS bilayer thin film possess higher FF compared to that based on the CsPbI₂Br:xNd³⁺ thin film, which possesses higher FF compared to that based on pristine CsPbI₂Br thin film.

Figure 7d presents the shelf stability of unencapsulated PSCs, which are stored in the glovebox with nitrogen atmosphere at room temperature. After ~1500 h, the PSCs based on pristine CsPbI₂Br thin-film decays 82% of their initial PCE value. The PSCs based on the CsPbI₂Br:xNd³⁺ thin film and CsPbI₂Br/LiSPS bilayer thin film maintain ~50% of their initial PCE values, whereas the PSCs based on the CsPbI₂Br:xNd³⁺/LiSPS bilayer thin film keeps ~83% of their initial PCE value at the same period. Boosted stability observed from the PSCs based on the CsPbI₂Br:xNd³⁺ thin film is due to the high quality of the CsPbI₂Br:xNd³⁺ thin film, and the dramatically enhanced stability of the PSCs based on the CsPbI₂Br:xNd³⁺/LiSPS bilayer thin film is attributed to the LiSPS interface passivation layer.

It is also found that the PSCs based on the CsPbI₂Br:xNd³⁺/ LiSPS bilayer thin film possess high reproducibility (Figure S6). Such high reproducibility is ascribed to both enlarged crystal sizes of the CsPbI₂Br:Nd³⁺ thin film and the interface passivation by the LiSPS layer.

CONCLUSIONS

In summary, we reported novel all-inorganic perovskites, where Pb²⁺ at the B-site was partially heterovalently substituted by Nd³⁺. It was found that the CsPbI₂Br:xNd³⁺ thin films possessed blue-shifted absorption and photoluminescence spectra, enlarged crystal sizes, enhanced charge carrier mobilities, and superior crystallinity. As a result, perovskite solar cells (PSCs) based on the CsPbI2Br:xNd3+ thin films exhibited more than 20% enhanced power conversion efficiency (PCE) as compared with that based on pristine CsPbI₂Br thin film. To further boost the device performance of PSCs, solution-processed LiSPS was utilized as the interface passivation layer. The PSCs based on the CsPbI₂Br:xNd³⁺/ LiSPS bilayer thin film exhibited reduced charge extraction lifetime and suppressed charge carrier recombination, resulting in 14% enhanced PCEs compared to that based on the CsPbI₂Br:xNd³⁺ thin film. Moreover, the PSCs based on the

CsPbI₂Br:xNd³⁺/LiSPS bilayer thin film possessed dramatically boosted stability. All these results demonstrated that we developed a facile way to approach high-performance PSCs by all-inorganic perovskites.

ASSOCIATED CONTENT

Supporting Information

The Supporting Information is available free of charge at https://pubs.acs.org/doi/10.1021/acsami.2c02023.

XPS spectroscopy, distribution of the perovskite crystal sizes, J-V characteristics, transient photocurrent, capacitance versus frequency characteristics and reproducibility of perovskite solar cells, and the PSCs with different thicknesses of the LiSPS interface passivation layer (PDF)

AUTHOR INFORMATION

Corresponding Author

Xiong Gong - School of Polymer Science and Polymer Engineering and Department of Chemical, Biomolecular and Corrosion Engineering, College of Engineering and Polymer Science, The University of Akron, Akron, Ohio 44325, United States; orcid.org/0000-0001-6525-3824; Email: xgong@uakron.edu; Fax: (330) 972-3406

Authors

Lening Shen - School of Polymer Science and Polymer Engineering, The University of Akron, Akron, Ohio 44325, United States

Yongrui Yang - School of Polymer Science and Polymer Engineering, The University of Akron, Akron, Ohio 44325, United States

Tao Zhu - School of Polymer Science and Polymer Engineering, The University of Akron, Akron, Ohio 44325, United States

Lei Liu - School of Polymer Science and Polymer Engineering, The University of Akron, Akron, Ohio 44325, United States

Jie Zheng - Department of Chemical, Biomolecular and Corrosion Engineering, College of Engineering and Polymer Science, The University of Akron, Akron, Ohio 44325, United States

Complete contact information is available at: https://pubs.acs.org/10.1021/acsami.2c02023

Notes

The authors declare no competing financial interest.

ACKNOWLEDGMENTS

The authors acknowledge the National Science Foundation (Grant ECCS/EPMD1903303) for financial support.

REFERENCES

(1) Kojima, A.; Teshima, K.; Shirai, Y.; Miyasaka, T. Organometal Halide Perovskites as Visible-Light Sensitizers for Photovoltaic Cells. J. Am. Chem. Soc. 2009, 131, 6050-6051.

(2) Wehrenfennig, C.; Eperon, G. E.; Johnston, M. B.; Snaith, H. J.; Herz, L. M. High Charge Carrier Mobilities and Lifetimes in Organolead Trihalide Perovskites. Adv. Mater. 2014, 26, 1584-1589. (3) Shi, D.; Adinolfi, V.; Comin, R.; Yuan, M.; Alarousu, E.; Buin, A.; Chen, Y.; Hoogland, S.; Rothenberger, A.; Katsiev, K.; et al. Low Trap-State Density and Long Carrier Diffusion in Organolead Trihalide Perovskite Single Crystals. Science 2015, 347, 519-522.

- (4) Xiong, J.; Yang, B.; Wu, R.; Cao, C.; Huang, Y.; Liu, C.; Hu, Z.; Huang, H.; Gao, Y.; Yang, J. Efficient and Non-Hysteresis CH₃NH₃PbI₃/PCBM Planar Heterojunction Solar Cells. *Org. Electron.* **2015**, *24*, 106–112.
- (5) Xu, W.; Zheng, L.; Zhang, X.; Cao, Y.; Meng, T.; Wu, D.; Liu, L.; Hu, W.; Gong, X. Efficient Perovskite Solar Cells Fabricated by Co Partially Substituted Hybrid Perovskite. *Adv. Energy Mater.* **2019**, 9, 1902152.
- (6) Wang, K.; Zheng, L.; Zhu, T.; Yao, X.; Yi, C.; Zhang, X.; Cao, Y.; Liu, L.; Hu, W.; Gong, X. Efficient Perovskite Solar Cells by Hybrid Perovskites Incorporated with Heterovalent Neodymium Cations. *Nano Energy* **2019**, *61*, 352–360.
- (7) Zhu, T.; Shen, L.; Xun, S.; Sarmiento, J. S.; Yang, Y.; Zheng, L.; Li, H.; Wang, H.; Bredas, J.-L.; Gong, X. High-Performance Ternary Perovskite-Organic Solar Cells. *Adv. Mater.* **2022**, *34*, 2109348.
- (8) Nrel, N. Best Research-Cell Efficiency Chart. U.S. Department of Energy, 2019.
- (9) Aharon, S.; Dymshits, A.; Rotem, A.; Etgar, L. Temperature Dependence of Hole Conductor Free Formamidinium Lead Iodide Perovskite Based Solar Cells. *J. Mater. Chem. A* **2015**, *3*, 9171–9178.
- (10) Eperon, G. E.; Stranks, S. D.; Menelaou, C.; Johnston, M. B.; Herz, L. M.; Snaith, H. J. Formamidinium Lead Trihalide: a Broadly Tunable Perovskite for Efficient Planar Heterojunction Solar Cells. *Energy Environ. Sci.* **2014**, *7*, 982–988.
- (11) Shen, L.; Zhu, T.; Zhang, X.; Gong, K.; Wang, H.; Gong, X. Bulk Heterojunction Perovskite Solar Cells Incorporated with p-Type Low Optical Gap Conjugated Polymers. *Nano Energy* **2022**, 93, 106907.
- (12) Eperon, G. E.; Paternò, G. M.; Sutton, R. J.; Zampetti, A.; Haghighirad, A. A.; Cacialli, F.; Snaith, H. J. Inorganic Caesium Lead Iodide Perovskite Solar Cells. *J. Mater. Chem. A* **2015**, *3*, 19688–19695.
- (13) Moller, C. K. Crystal Structure and Photoconductivity of Cæsium Plumbohalides. *Nature* **1958**, *182*, 1436.
- (14) Saidaminov, M. I.; Haque, M. A.; Almutlaq, J.; Sarmah, S.; Miao, X. H.; Begum, R.; Zhumekenov, A. A.; Dursun, I.; Cho, N.; Murali, B.; et al. Inorganic Lead Halide Perovskite Single Crystals: Phase-Selective Low-Temperature Growth, Carrier Transport Properties, and Self-Powered Photodetection. *Adv. Opt. Mater.* **2017**, *5*, 1600704
- (15) Beal, R. E.; Slotcavage, D. J.; Leijtens, T.; Bowring, A. R.; Belisle, R. A.; Nguyen, W. H.; Burkhard, G. F.; Hoke, E. T.; McGehee, M. D. Cesium Lead Halide Perovskites with Improved Stability for Tandem Solar Cells. *J. Phys. Chem. Lett.* **2016**, *7*, 746–751.
- (16) Luo, P.; Xia, W.; Zhou, S.; Sun, L.; Cheng, J.; Xu, C.; Lu, Y. Solvent Engineering for Ambient-Air-Processed, Phase-Stable CsPbI₃ in Perovskite Solar Cells. *J. Phys. Chem. Lett.* **2016**, *7*, 3603–3608.
- (17) Nam, J. K.; Chai, S. U.; Cha, W.; Choi, Y. J.; Kim, W.; Jung, M. S.; Kwon, J.; Kim, D.; Park, J. H. Potassium Incorporation for Enhanced Performance and Stability of Fully Inorganic Cesium Lead Halide Perovskite Solar Cells. *Nano Lett.* **2017**, *17*, 2028–2033.
- (18) Sutton, R. J.; Eperon, G. E.; Miranda, L.; Parrott, E. S.; Kamino, B. A.; Patel, J. B.; Hörantner, M. T.; Johnston, M. B.; Haghighirad, A. A.; Moore, D. T.; Snaith, H. J. Bandgap-Tunable Cesium Lead Halide Perovskites with High Thermal Stability for Efficient Solar Cells. *Adv. Energy Mater.* **2016**, *6*, 1502458.
- (19) Lau, C. F. J.; Deng, X.; Ma, Q.; Zheng, J.; Yun, J. S.; Green, M. A.; Huang, S.; Ho-Baillie, A. W. CsPbIBr₂ Perovskite Solar Cell by Spray-Assisted Deposition. *ACS Energy Lett.* **2016**, *1*, 573–577.
- (20) Kulbak, M.; Cahen, D.; Hodes, G. How Important Is the Organic Part of Lead Halide Perovskite Photovoltaic Cells? Efficient CsPbBr₃ Cells. *J. Phys. Chem. Lett.* **2015**, *6*, 2452–2456.
- (21) Luo, P.; Zhou, Y.; Zhou, S.; Lu, Y.; Xu, C.; Xia, W.; Sun, L. Fast Anion-Exchange from CsPbI₃ to CsPbBr₃ via Br₂-Vapor-Assisted Deposition for Air-Stable All-Inorganic Perovskite Solar Cells. *Chem. Eng. J.* **2018**, 343, 146–154.
- (22) Zhou, S.; Tang, R.; Yin, L. Slow-Photon-Effect-Induced Photoelectrical-Conversion Efficiency Enhancement for Carbon-

- Quantum-Dot-Sensitized Inorganic CsPbBr₃ Inverse Opal Perovskite Solar Cells. Adv. Mater. 2017, 29, 1703682.
- (23) Liu, Z.; Sun, B.; Liu, X.; Han, J.; Ye, H.; Shi, T.; Tang, Z.; Liao, G. Efficient Carbon-Based CsPbBr₃ Inorganic Perovskite Solar Cells by Using Cu-Phthalocyanine as Hole Transport Material. *Nano-Micro Lett.* **2018**, *10*, 34.
- (24) Boix, P. P.; Nonomura, K.; Mathews, N.; Mhaisalkar, S. G. Current Progress and Future Perspectives for Organic/Inorganic Perovskite Solar Cells. *Mater. Today* **2014**, *17*, 16–23.
- (25) Liu, C.; Li, W.; Zhang, C.; Ma, Y.; Fan, J.; Mai, Y. All-Inorganic CsPbI₂Br Perovskite Solar Cells with High Efficiency Exceeding 13%. *J. Am. Chem. Soc.* **2018**, *140*, 3825–3828.
- (26) Ye, Q.; Zhao, Y.; Mu, S.; Ma, F.; Gao, F.; Chu, Z.; Yin, Z.; Gao, P.; Zhang, X.; You, J. Cesium Lead Inorganic Solar Cell with Efficiency beyond 18% via Reduced Charge Recombination. *Adv. Mater.* **2019**, *31*, 1905143.
- (27) Liu, C.; Yang, Y.; Zhang, C.; Wu, S.; Wei, L.; Guo, F.; Arumugam, G. M.; Hu, J.; Liu, X.; Lin, J.; Schropp, R. E. I.; Mai, Y. Tailoring C₆₀ for Efficient Inorganic CsPbI₂Br Perovskite Solar Cells and Modules. *Adv. Mater.* **2020**, *32*, 1907361.
- (28) Saliba, M.; Matsui, T.; Domanski, K.; Seo, J. Y.; Ummadisingu, A.; Zakeeruddin, S. M.; Correa-Baena, J. P.; Tress, W. R.; Abate, A.; Hagfeldt, A.; Grätzel, M. Incorporation of rubidium cations into perovskite solar cells improves photovoltaic performance. *Science* **2016**, 354, 206–209.
- (29) Navas, J.; Sanchez-Coronilla, A.; Gallardo, J. J.; Cruz Hernandez, N.; Pinero, J. C.; Alcantara, R.; Fernandez-Lorenzo, C.; De los Santos, D. M.; Aguilar, T.; Martin-Calleja, J. New insights into organic—inorganic hybrid perovskite CH₃NH₃PbI₃ nanoparticles. an experimental and theoretical study of doping in Pb²⁺ sites with Sn²⁺, Sr²⁺, Cd²⁺ and Ca²⁺. *Nanoscale* **2015**, *7*, 6216–6229.
- (30) Zheng, L. Y.; Zhu, T.; Xu, W. Z.; Zheng, J.; Liu, L.; Gong, X. Ultrasensitive perovskite photodetectors by Co partially substituted hybrid perovskite. *ACS Sust. Chem. Eng.* **2018**, *6*, 12055–12060.
- (31) Wang, J. T.W.; Wang, Z.; Pathak, S.; Zhang, W.; deQuilettes, D. W.; Wisnivesky-Rocca-Rivarola, F.; Huang, J.; Nayak, P. K.; Patel, J. B.; Yusof, H. A. M.; Vaynzof, Y.; Zhu, R.; et al. Efficient perovskite solar cells by metal ion doping. *Ener. Environ. Sci.* **2016**, *9*, 2892–2901.
- (32) Zheng, L. Y.; Wang, K.; Zhu, T.; Liu, L.; Zheng, J.; Gong, X. Solution-processed ultrahigh detectivity photodetectors by hybrid perovskite incorporated with heterovalent neodymium cations. *ACS Omega* **2019**, *4*, 15873–15878.
- (33) Remya, K. P.; Amirthapandian, S.; Raja, M. M.; Viswanathan, C.; Ponpandian, N. Effect of Yb substitution on room temperature magnetic and dielectric properties of bismuth ferrite nanoparticles. *J. Appl. Phys.* **2016**, *120*, 134304.
- (34) Kazhugasalamoorthy, S.; Jegatheesan, P.; Mohandoss, R.; Giridharan, N. V.; Karthikeyan, B.; Joseyphus, R. J.; Dhanuskodi, S. Investigations on the Properties of Pure and Rare Earth Modified Bismuth Ferrite Ceramics. *J. Alloys Compd.* **2010**, 493, 569–572.
- (35) Yamamoto, H.; Okamoto, S.; Kobayashi, H. Luminescence of Rare-Earth Ions in Perovskite-Type Oxides: from Basic Research to Applications. *J. Lumin.* **2002**, *100*, 325–332.
- (36) de Figueiredo, A. T.; Longo, V. M.; da Silva, R. O.; Mastelaro, V. R.; Mesquita, A.; Franco, R. W. A.; Varela, J. A.; Longo, E. Structural XANES Characterization of Ca_{0.99}Sm_{0.01}TiO₃ Perovskite and Correlation with Photoluminescence Emission. *Chem. Phys. Lett.* **2012**, *544*, 43–48.
- (37) Verma, V. Structural, Electrical and Magnetic Properties of Rare-Earth and Transition Element co-Doped Bismuth Ferrites. *J. Alloys Compd.* **2015**, *641*, 205–209.
- (38) Wang, Y.; Nan, C. W. Effect of Tb Doping on Electric and Magnetic Behavior of BiFeO₃ Thin Films. *J. Appl. Phys.* **2008**, *103*, 024103
- (39) Singh, S. K. Structural and Electrical Properties of Sm-Substituted BiFeO₃ Thin Films Prepared by Chemical Solution Deposition. *Thin Solid Films* **2013**, *527*, 126–132.

- (40) Yan, F.; Lai, M. O.; Lu, L.; Zhu, T. J. Enhanced Multiferroic Properties and Valence Effect of Ru-Doped BiFeO₃ Thin Films. *J. Phys. Chem. C* **2010**, *114*, 6994–6998.
- (41) Steckl, A. J.; Zavada, J. M. Optoelectronic Properties and Applications of Rare-Earth-Doped GaN. MRS Bull. 1999, 24, 33–38.
- (42) Sun, Y.; Thiel, C. W.; Cone, R. L.; Equall, R. W.; Hutcheson, R. L. Recent Progress in Developing New Rare Earth Materials for Hole Burning and Coherent Transient Applications. *J. Lumin.* **2002**, *98*, 281–287.
- (43) Liu, Q.; Dai, J.; Zhang, X.; Zhu, G.; Liu, Z.; Ding, G. Perovskite-type transparent and conductive oxide films: Sb-and Nd-doped SrSnO₃. *Thin Solid Films* **2011**, *519*, 6059–6063.
- (44) Mitzi, D. B.; Liang, K. Preparation and Properties of $(C_4H_9NH_3)_2EuI_4$: A Luminescent Organic-Inorganic Perovskite with a Divalent Rare-Earth Metal Halide Framework. *Chem. Mater.* 1997, 9, 2990–2995.
- (45) Müller, K. A.; Kool, T. W. Properties of Perovskites and Other Oxides; World Scientific, 2010.
- (46) Jiang, Z.; Li, X.; Strzalka, J.; Sprung, M.; Sun, T.; Sandy, A. R.; Narayanan, S.; Lee, D. R.; Wang, J. The Dedicated High-Resolution Grazing-Incidence X-ray Scattering Beamline 8-ID-E at the Advanced Photon Source. *J. Synchrotron Radiat.* **2012**, *19*, 627–636.
- (47) Hu, Y.; Qiu, T.; Bai, F.; Miao, X.; Zhang, S. Enhancing Moisture-Tolerance and Photovoltaic Performances of FAPbI₃ by Bismuth Incorporation. *J. Mater. Chem. A* **2017**, *5*, 25258–25265.
- (48) Zhang, J.; Shang, M.; Wang, P.; Huang, X.; Xu, J.; Hu, Z.; Zhu, Y.; Han, L. n-Type Doping and Energy States Tuning in $CH_3NH_3Pb_{1-x}Sb_{2x/3}I_3$ Perovskite Solar Cells. *ACS Energy Lett.* **2016**, *1* (3), 535–541.
- (49) Liu, W.; Liu, N.; Ji, S.; Hua, H.; Ma, Y.; Hu, R.; Zhang, J.; Chu, L.; Li, X.; Huang, W. Perfection of Perovskite Grain Boundary Passivation by Rhodium Incorporation for Efficient and Stable Solar Cells. *Nano-Micro Lett.* **2020**, *12*, 119.
- (50) Xie, Y.; Peng, B.; Bravic, I.; Yu, Y.; Dong, Y.; Liang, R.; Ou, Q.; Monserrat, B.; Zhang, S. Highly Efficient Blue-Emitting CsPbBr3 Perovskite Nanocrystals through Neodymium Doping. *Adv. Sci.* **2020**, 7, 2001698.
- (51) Xiong, J.; Cao, S.; Xing, K.; Chen, M.; Zeng, R.; Zou, B.; Zhao, J. Enhanced Photoluminescence Efficiencies of CsPbCl_{3-x}Br_x Nanocrystals by Incorporating Neodymium Ions. *J. Lumin.* **2022**, 243, 118658.
- (52) Taheri-Ledari, R.; Gharibi, S.; Maleki, A.; Akin, S.; Shalan, A. E. Neodymium and Praseodymium Doped Perovskite Materials for Highly Stable CuInS2-HTL based Perovskite Solar Cells. *Energy Technol.* **2022**, 2100936.
- (53) Bube, R. H. Trap Density Determination by Space-Charge-Limited Currents. J. Appl. Phys. 1962, 33, 1733-1737.
- (54) Wang, K.; Liu, C.; Yi, C.; Chen, L.; Zhu, J.; Weiss, R.; Gong, X. Efficient Perovskite Hybrid Solar Cells via Ionomer Interfacial Engineering. *Adv. Funct. Mater.* **2015**, *25*, 6875–6884.
- (55) van Reenen, S.; Kemerink, M.; Snaith, H. J. Modeling Anomalous Hysteresis in Perovskite Solar Cells. *J. Phys. Chem. Lett.* **2015**, *6*, 3808–3814.
- (56) Seifter, J.; Sun, Y.; Heeger, A. J. Transient Photocurrent Response of Small-Molecule Bulk Heterojunction Solar Cells. *Adv. Mater.* **2014**, *26*, 2486–2493.
- (57) Yun, J. H.; Lee, I.; Kim, T. S.; Ko, M. J.; Kim, J. Y.; Son, H. J. Synergistic Enhancement and Mechanism Study of Mechanical and Moisture Stability of Perovskite Solar Cells Introducing Polyethylene-imine into the CH₃NH₃PbI₃/HTM Interface. *J. Mater. Chem. A* **2015**, 3, 22176–22182.
- (58) Murgatroyd, P. N. Theory of Space-Charge-Limited Current Enhanced by Frenkel Effect. J. Phys. D: Appl. Phys. 1970, 3, 151.
- (59) Street, R.; Schoendorf, M.; Roy, A.; Lee, J. Interface State Recombination in Organic Solar Cells. *Phys. Rev. B* **2010**, *81*, 205307. (60) Cowan, S. R.; Roy, A.; Heeger, A. J. Recombination in Polymer-Fullerene Bulk Heterojunction Solar Cells. *Phys. Rev. B* **2010**, *82*,

245207.

- (61) Xu, W.; Yao, X.; Meng, T.; Wang, K.; Huang, F.; Gong, X.; Cao, Y. Perovskite Hybrid Solar Cells with a Fullerene Derivative Electron Extraction Layer. *J. Mater. Chem. C* **2017**, *5*, 4190–4197.
- (62) Koster, L. J. A.; Mihailetchi, V. D.; Ramaker, R.; Blom, P. W. Light Intensity Dependence of Open-Circuit Voltage of Polymer: Fullerene Solar Cells. *Appl. Phys.s Lett.* **2005**, *86*, 123509.
- (63) Zhu, T.; Zheng, L.; Xiao, Z.; Meng, X.; Liu, L.; Ding, L.; Gong, X. Functionality of Non-Fullerene Electron Acceptors in Ternary Organic Solar Cells. *Sol. RRL* **2019**, *3*, 1900322.
- (64) Li, Z.; Wang, W.; Greenham, N. C.; McNeill, C. R. Influence of Nanoparticle Shape on Charge Transport and Recombination in Polymer/Nanocrystal Solar Cells. *Phys. Chem. Chem. Phys.* **2014**, *16*, 25684–25693.

□ Recommended by ACS

Ethylenediammonium-Based "Hollow" Pb/Sn Perovskites with Ideal Band Gap Yield Solar Cells with Higher Efficiency and Stability

Weijun Ke, Mercouri G. Kanatzidis, et al.

MAY 07, 2019

JOURNAL OF THE AMERICAN CHEMICAL SOCIETY

READ 🖸

Design, Synthesis, and Photocatalytic Application of Moisture-Stable Hybrid Lead-Free Perovskite

Guang-Ning Liu, Cuncheng Li, et al.

NOVEMBER 20, 2020

ACS APPLIED MATERIALS & INTERFACES

READ 🗹

Cesium Lead Mixed-Halide Perovskites for Low-Energy Loss Solar Cells with Efficiency Beyond 17%

Haoran Wang, Shengzhong Frank Liu, et al.

JULY 31, 2019

CHEMISTRY OF MATERIALS

READ [7]

Thymine as a Biocompatible Surface Passivator for a Highly Efficient and Stable Planar Perovskite Solar Cell

Yanan Zhao, Hua Bai, et al.

APRIL 12, 2021

ACS APPLIED ENERGY MATERIALS

READ 🗹

Get More Suggestions >